Impact of trench retreat rate on initiating focused back-arc extension within a mobile overriding plate

Zhibin Lei[1], J. H. Davies[1]

[1]School of Earth and Environmental Sciences, Cardiff University, Cardiff, CF10 3AT, UK

Correspondence to: Zhibin Lei (leiz2@cardiff.ac.uk)

Abstract

Rapid trench retreat, or slab roll-back, is often observed in subduction zones where active and focused back-arc extension develops. However, the correlation between trench retreat rate and back-arc extension has not been rigorously tested. Here we study the correlation by investigating a series of 2-D thermo-mechanical and internally driven numerical models with a mobile overriding plate in set-ups that lead to a wide range of trench retreat rate. The results produced three grades of localised back-arc stretching states as the trench retreat rate increases: i) minor extension with observable but not significant thinning of the thermal lithosphere; ii) rifting extension with hot mantle thermally intruded upward to the surface; iii) new spreading seafloor with thin lithosphere. We find that it takes a minimum trench retreat rate to initiate rifting extension in the back-arc. The extension is driven by the non-uniform basal drag of the trenchward mantle wedge flow due to rapid trench retreat. The results could potentially be used to explain the southward decreasing stretching state along the Lau-Havre-Taupo back-arc system where trench retreat rate decreases southward as well. On the other hand, in the models we find that an older subducting plate leads to faster trench retreat rate, but this correlation only exists before the slab approaches the lower mantle. This matches well with the observation that the subducting plate age is always old (>55 Ma) in subduction zones with back-arc extension. It also explains why there is a poor correlation between the age of subducting plate and trench retreat rate because most slabs have already reached the lower mantle.

Keywords: subduction; trench retreat; back-arc; rifting; basal drag; numerical modeling.

Highlights:

1. Investigate dynamic internally driven subduction models with mobile overriding plate

2. Self-consistently produce high trench retreat rate and rifting, even in mobile plates

3. A minimum trench retreat rate is required to initiate rifting of the back-arc region

4. Back-arc extension arises from non-uniform basal drag induced by rapid trench retreat

1. Introduction

The extension observed within the overriding plate in different subduction zones varies, especially in the back-arc. The extension ranges from inactive extension with high heat flow, e.g. Southeast Aleutian Basin (Christeson and Barth, 2015), to a rifting ridge with thinning lithosphere, e.g. Central Andaman Basin, Taupo Volcanic Zone (Morley and Alvey, 2015; Parson and Wright, 1996), and further extended to the opening of a new oceanic floor, e.g. Sea of Japan, Lau Basin (Jolivet et al., 1994; Taylor et al., 1996). The extension plays a significant role in producing hazards (Kósik et al., 2020) and generating resources (Fouquet et al., 1991; Hessler and Sharman, 2018), but the underlying driving mechanism is poorly understood.

Observation of plate and trench motion shows that retreating trench correlates well with the existence of back-arc extension except for some cases where trench retreat rate is lower than 5 cm/yr (Heuret and Lallemand, 2005; Schellart et al., 2008). A general explanation for this correlation is that the overriding plate extends to accommodate the void that trench retreat leaves. In detail, two driving mechanisms have been proposed: trench retreat generates strong convection currents (poloidal and toroidal flow) that transmits non-uniform basal traction upon the overriding plate (Sleep and Toksöz, 1971); and trench suction at the subduction zone interface pulls the overriding plate (Elsasser, 1971).

Further observations of subducting systems with a high trench retreat rate shows that a localised extension often develops in the overriding plate. For example, the trench retreat rate at Tonga is ~16 cm/yr where we observe spreading ridge and opening seafloor (Bevis et al., 1995). The correlation is supported by numerical and analogue investigations. Both trench retreat induced poloidal and toroidal flow components show a positive correlation with trench retreat rate (Funiciello et al., 2004; Stegman et al., 2006). Models with a higher trench retreat rate also correlates with higher strain rate in the overriding plate (Holt et al., 2015; Meyer & Schellart, 2013). On the other hand, previous research indicates that the trailing boundary condition and heterogeneity of the overriding plate also play important roles in affecting the degree of back-arc extension. Models with either a fixed overriding plate or an overriding plate containing an arbitrary weak zone are prone to produce rifting or spreading back-arc extension (Capitanio et al., 2010; Gerya et al., 2008; Hertgen et al., 2020; Nakakuki and Mura, 2013; Yang et al., 2019), while studies with a mobile and homogeneous (without an arbitrary weak zone) overriding plate often fail to produce an opening back-arc incorporating focused thinning lithosphere (Chen et al., 2016; Čížková and Bina, 2013; Schellart and Moresi, 2013). To summarise, rigorous investigation has not been done yet on the trench retreat rate’s role in initiating different extents of back-arc extension, especially within a mobile and homogeneous overriding plate.

In this research, we ran a series of 2-D thermo-mechanical and self-consistently driven models with a mobile overriding plate in set-ups that lead to a wide range of trench retreat rate. The results produced three different types of localised back-arc stretching states as the trench retreat rate increases: i) minor extension with observable but not significant thinning of the thermal lithosphere; ii) rifting extension with hot mantle thermally intruded upward to the surface; iii) new spreading seafloor with thin lithosphere. We find that a minimum trench retreat rate is needed to initiate rifting extension in the back-arc. The extension is driven by the non-uniform basal drag of the trenchward mantle wedge flow due to rapid trench retreat.

2. Methods

Extending the model setup of Garel et el. (2014), we ran a series of 2-D thermally-driven subduction models using the code Fluidity (Davies et al., 2011; Kramer et al., 2012), a finite-element control-volume computational modelling framework, with an adaptive mesh that can capture evolving changes with a maximum resolution of 0.4 km. To obtain a wide range of trench retreat rate for a mobile overriding plate, we vary the initial age of the subducting plate at the trench.

2.1 Governing equations

Under the Boussinesq approximation (McKenzie et al., 1974), the equations governing thermally driven subduction process are derived from conservation of mass, momentum, and energy, for an incompressible Stokes flow

$$\partial_i u_i = 0, \tag{1}$$

$$\partial_i \sigma_{ij} = -\Delta\rho g_j, \tag{2}$$

$$\frac{\partial T}{\partial t} + u_i \partial_i T = \kappa \partial_i^2 T, \tag{3}$$

in which u, g, σ, T, κ are the velocity, gravity, stress, temperature, and thermal diffusivity, respectively (Table 1). In particular, the full stress tensor σ_{ij} consists of deviatoric and lithostatic components via

$$\sigma_{ij} = \tau_{ij} - p\delta_{ij}, \tag{4}$$

where τ_{ij} represents the deviatoric stress tensor, p the dynamic pressure, and δ_{ij} the Kronecker delta function.

Table 1. Key parameters used in this research

Quantity	Symbol	Units	Value
Gravity	g	$m\ s^{-2}$	9.8
Gas constant	R	$J\ K^{-1}\ mol^{-1}$	8.3145
Mantle geothermal gradient	G	$K\ km^{-1}$	0.5 (UM) 0.3 (LM)
Thermal expansivity coefficient	α	K^{-1}	3×10^{-5}
Thermal diffusivity	κ	$m^2\ s^{-1}$	10^{-6}
Reference density	ρ_s	$kg\ m^{-3}$	3300
Cold, surface temperature	T_s	K	273
Hot, mantle temperature	T_m	K	1573
Maximum viscosity	μ_{max}	$Pa\ s$	10^{25}
Minimum viscosity	μ_{min}	$Pa\ s$	10^{18}
Diffusion Creep			
Activation energy	E	$kJ\ mol^{-1}$	300 (UM) 200 (LM)
Activation volume	V	$cm^3\ mol^{-1}$	4 (UM) 1.5 (LM)
Prefactor	A	$Pa^{-n}\ s^{-1}$	3.0×10^{-11} (UM) 6.0×10^{-17} (LM)
	n		1
Dislocation Creep (UM)			
Activation energy	E	$kJ\ mol^{-1}$	540
Activation volume	V	$cm^3\ mol^{-1}$	12
Prefactor	A	$Pa^{-n}\ s^{-1}$	5.0×10^{-16}
	n		3.5
Peierls Creep (UM)			
Activation energy	E	$kJ\ mol^{-1}$	540
Activation volume	V	$cm^3\ mol^{-1}$	10
Prefactor	A	$Pa^{-n}\ s^{-1}$	10^{-150}
	n		20
Yield Strength Law			
Surface yield strength	τ_0	MPa	2
Friction coefficient	f_c		0.2
	$f_{c,weak}$		0.02 (weak layer)
Maximum yield strength	$\tau_{y,max}$	MPa	10,000

The deviatoric stress tensor and strain rate tensor $\dot{\varepsilon}_{ij}$ are related according to

$$\tau_{ij} = 2\mu\dot{\varepsilon}_{ij} = \mu\left(\partial_j u_i + \partial_i u_j\right), \tag{5}$$

with μ the viscosity. The density difference due to temperature is defined as

$$\Delta\rho = -\alpha\rho_s(T - T_s), \tag{6}$$

where α is the coefficient of thermal expansion, ρ_s is the reference density at the surface temperature T_s (Table 1).

2.2 Rheology

The governing rheological laws are identical throughout the model domain, though the rheology parameters we use may differ to match different deformation mechanisms observed at different depths in the Earth. In detail, a uniform composite viscosity is used to take account of four deformation mechanisms under different temperature-pressure conditions: diffusion creep, dislocation creep, Peierls mechanism, and yielding (Garel et al., 2014). The effective composite viscosity in the computational domain is given by

$$\mu = \left(\frac{1}{\mu_{diff}} + \frac{1}{\mu_{disl}} + \frac{1}{\mu_P} + \frac{1}{\mu_y}\right)^{-1}, \tag{7}$$

where μ_{diff}, μ_{disl}, μ_y define the creep viscosity following

$$\mu_{diff/disl/P} = A^{-\frac{1}{n}} exp\left(\frac{E+PV}{nRT_r}\right)\dot{\varepsilon}_{II}^{\frac{1-n}{n}}, \tag{8}$$

in which A is a prefactor, n the stress component, E the activation energy, P the lithostatic pressure, V the volume, R the gas constant, T_r the temperature obtained by adding an adiabatic gradient of 0.5 K/km in the upper mantle and 0.3 K/km in the lower mantle to the Boussinesq solution (Fowler, 2005), $\dot{\varepsilon}_{II}$ the second invariant of the strain rate tensor. While the fourth deformation mechanism, yielding, is defined by a brittle-failure type yield-stress law as

$$\mu_y = \frac{\tau_y}{2\dot{\varepsilon}_{II}}, \tag{9}$$

with μ_y the yielding viscosity and τ_y the yield strength. τ_y is determined by

$$\tau_y = min(\tau_0 + f_c P, \tau_{y,max}), \tag{10}$$

with τ_0 the surface yield strength, f_c the friction coefficient, P the lithostatic pressure, and $\tau_{y,max}$ the maximum yield strength (Table 1). Note the weak zone, a 5 km thick region on top of the subducting plate, has the same rheology, except its value of f_c is one tenth, and its maximum viscosity is 10^{20} Pa s. We note that for all models in this research there is no arbitrary weak zone emplaced in the initial overriding plate.

2.3 Model setup

Following Garel et al., 2014, we run spatially large models where the computational domain is 10000 km by 2900 km, with x (width) coordinates and z (depth) coordinates extending from the surface to the bottom of the lower mantle. Such a wide domain reduces the influence of side and bottom boundary conditions (Chertova et al., 2012). The thermal boundary conditions at the surface and bottom are defined by two isothermal values: $T = T_s$ and $T = T_m$ for surface and base of lower mantle respectively, while the sidewalls are insulating. As for velocity boundary conditions, a free-surface is applied at the top boundary to enable trench mobility, while the other boundaries are free-slip.

Age_{SP}^{0} and Age_{OP}^{0} represent the initial ages of subducting plate and overriding plate at the trench, which starts in the middle of the surface. Laterally on the surface, the age of both plates increases linearly with its distance away from the mid-ocean ridge on either side. While vertically, the age of plate at surface defines the initial thermal structure through a half-space cooling model (Turcotte and Schubert, 2002),

$$T(x,z) = T_s + (T_m - T_s)erf\left(\frac{z}{2\sqrt{\kappa Age^0(x)}}\right), \tag{11}$$

with x the distance away from the mid-ocean ridge, z the depth, κ the thermal diffusivity. The thermal lithosphere is defined as the material colder than 1300 K.

The free surface boundary condition together with the mid-ocean ridge setup allow the subducting slab, overriding plate and trench to move freely as subduction evolves. To allow for a self-driven subduction without implementing external forces, the subducting plate is set up with a bend into the mantle and a 5 km thick low-viscosity decoupling layer on the top. The initial bending radius is 250 km and the slab bends over 77 degrees from the trench (Figure 1).

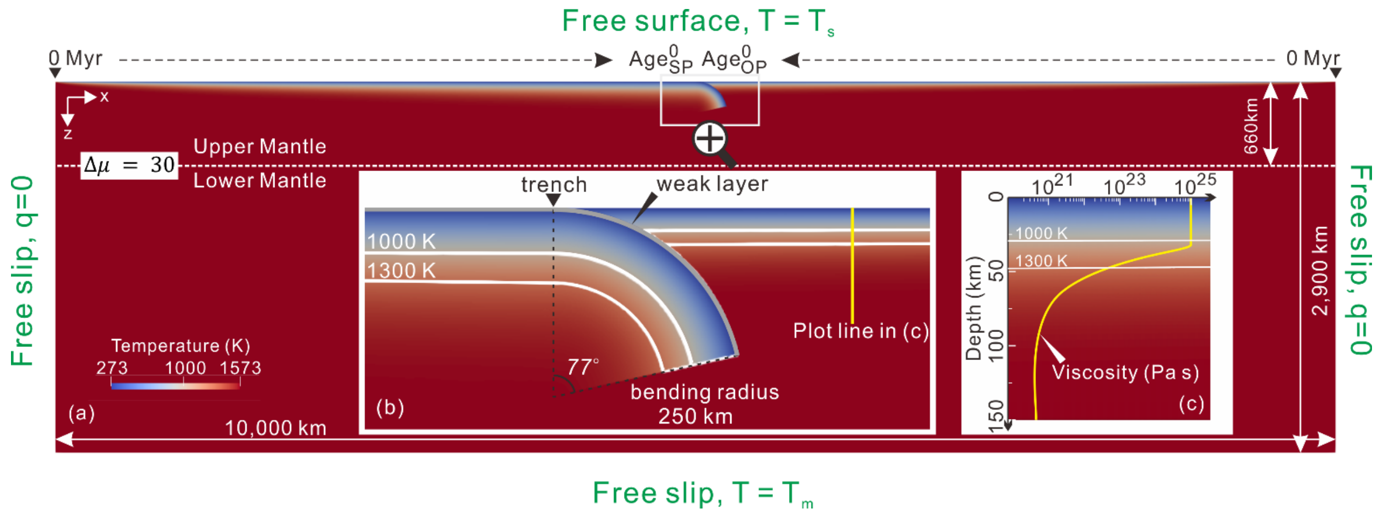

Figure 1. Model geometry and initial setup illustrated with the initial temperature field as the background. Age_{SP}^{0} and Age_{OP}^{0} represent the initial ages of subducting plate and overriding plate at trench. The viscosity jump ($\Delta\mu$) between upper and lower mantle at 660km transition zone is set up with a fixed value of 30. The trench is recognised as the position where the overriding plate meets the weak layer coating the subducting plate at the surface. a) The whole computational domain. b) Enlarged area of trench zone where bending slab meets flat overriding plate. A 5 km thick weak layer is set up on top of the subducting slab to facilitate decoupling. 1100 K and 1300 K isotherms are marked in while lines. c) Vertical profile of viscosity against depth within the overriding plate. The plot line is 400 km away from the initial trench.

2.4 Modify the rate of trench retreat

Trench retreat rate is related to multiple factors. Numerical investigations have shown that older subducting plate or higher slab density (Alsaif et al., 2020; Garel et al., 2014), narrower trench width (Schellart et al., 2011; Stegman et al., 2006), the inclusion of overriding plate and its aspect ratio (Butterworth et al., 2012; Capitanio et al., 2010) , younger overriding plate or thinner overriding plate (Garel et al., 2014; Hertgen et al., 2020), and less slab resistance to bending (Di Giuseppe et al., 2008) could all contribute to stronger trench retreat. While a higher viscosity jump at the mantle transition zone (Čížková and Bina, 2013; Garel et al., 2014), and a stress-dependent mantle viscosity (Holt & Becker, 2017) could reduce the rate of trench retreat.

Of all the parameters, the plate age turns out to be a concise and efficient parameter to obtain a wide range of trench retreat rate in our model set-up. In detail, we only modify the initial plate ages

(Age_{SP}^0 and Age_{OP}^0) at the trench (Table 2), which varies the net negative buoyancy of the hanging slab and determines the maximum trench retreat rate potential during subduction. Meanwhile, several diagnostics were used to monitor the trench motion during the 10 Myr long simulations. Two series of models, each series with the same Age_{OP}^0 and a growing Age_{SP}^0, are simulated to demonstrate the role trench retreat rate may play in generating different extent of localised extension in the back-arc region.

Table 2. List of representative models with key variables governing trench retreat rate and diagnostics monitoring the trench motion and stretching state of the overriding plate.

Model name	Age_{SP}^0 (Myr)	Age_{OP}^0 (Myr)	H_{SP}^0 (km)	H_{OP}^0 (km)	t_{660} (Myr)	$\left\|\triangle x_{trench}^{0-t_{660}}\right\|$ (km)	$\left\|u_{max}^{0-t_{660}}\right\|$ (cm/yr)	$\left\|\overline{u_{trench}^{0-t_{660}}}\right\|$ (cm/yr)	Back-arc stretching state
SP80_OP20	80	20	89	45	3.8	138	11	3.6	i
SP90_OP20	90	20	94	45	3.5	160	14	4.6	i
SP100_OP20	100	20	100	45	3.2	200	19	6.3	ii
SP125_OP20	125	20	111	45	2.8	340	65	12.1	iii
SP150_OP20	150	20	122	45	2.5	390	113	15.6	iii
SP100_OP25	100	25	100	50	4.1	145	10	3.5	i
SP125_OP25	125	25	111	50	3.7	168	14	4.5	i
SP150_OP25	150	25	122	50	3.5	200	20	5.7	i
SP175_OP25	175	25	132	50	3.3	250	27	7.6	ii
SP200_OP25	200	25	141	50	3.1	375	96	12.1	iii

Models are named as follows, e.g. SP80_OP20 corresponds to initial subducting plate age at the trench of 80 Myr and 20 Myr for overriding plate. H_{SP}^0 and H_{OP}^0 are the initial thermal lithosphere thickness, marked by 1300 K isotherm, of the subducting plate and overriding plate at trench separately. t_{660} equals how much time the subducting plate takes to sink to 660km depth. $\left|\triangle x_{trench}^{0-t_{660}}\right|$ is the total trench retreat in the period of t_{660}. $\left|u_{max}^{0-t_{660}}\right|$ and $\left|\overline{u_{trench}^{0-t_{660}}}\right|$ are the magnitude of maximum and average trench retreat rate recorded during t_{660}. The code i, ii and iii describing the back-arc stretching state of the overriding plate represents minor extension, rifting and new spreading seafloor, respectively.

With a wide range of trench retreat rates achieved, we will be able to investigate its influence on the formation of different extents of extension within the overriding plate.

3. Results

3.1 Trench retreat rate through time

Self-consistent subduction, in most numerical and analogue models, starts with a non-steady state where negative buoyancy pulls the slab into the deeper mantle (eg. Capitanio et al., 2010; Gerya et al., 2008; Schellart and Moresi, 2013). Meanwhile, trench retreat accelerates with time and reaches a maximum value ($u_{max}^{0-t_{660}}$) when the slab starts to interact with the lower mantle at t_{660} (Figure 2-a). During the interaction, the viscosity jump at ~660 km provides a balanced competing upward support to the sinking slab, as a result the trench retreat experiences an abrupt deceleration due to the reducing slab pull force. After this short period of adjustment, subduction enters the second stage, a near steady state where trench retreat rate keeps a constant magnitude at ~ 3 cm/yr for all the models.

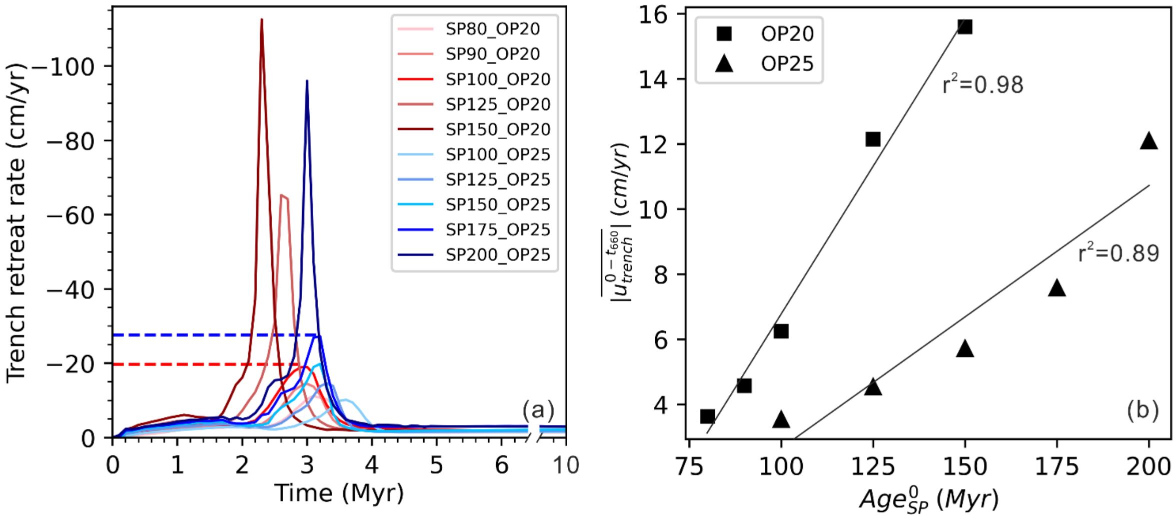

Figure 2. The motion of the trench through time and its Age_{OP}^{0} dependency during non-steady state subduction. a) Trench retreat rate through time. Negative value means that the trench is moving towards the subducting plate. The dashed lines of red and blue marks the $u_{max}^{0-t_{660}}$ for model SP100_OP20 and SP175_OP25 separately. b) Slab age dependency of diagnostic $\left|\overline{u_{trench}^{0-t_{660}}}\right|$ during non-steady state subduction.

For models with the same overriding plate setup, the average trench retreat rate over the first stage ($\left|\overline{u_{trench}^{0-t_{660}}}\right|$) is Age_{SP}^{0}-dependent during non-steady state subduction (Figure 2-b). However, this dependence fades away when the slab starts to interact with the lower mantle (Figure 2-a).

3.2 Subduction kinematics

Starting from our segmentation of the subduction into non-steady and steady state subduction, we investigate further to reveal more details of this model subduction system. Here using model SP175_OP25 as a case study, we characterise the whole process by illustrating the simultaneous dynamic evolution of temperature, horizontal component of the stress field, horizontal component of the velocity field, second invariant of strain rate, and magnitude of viscosity (Figure 3).

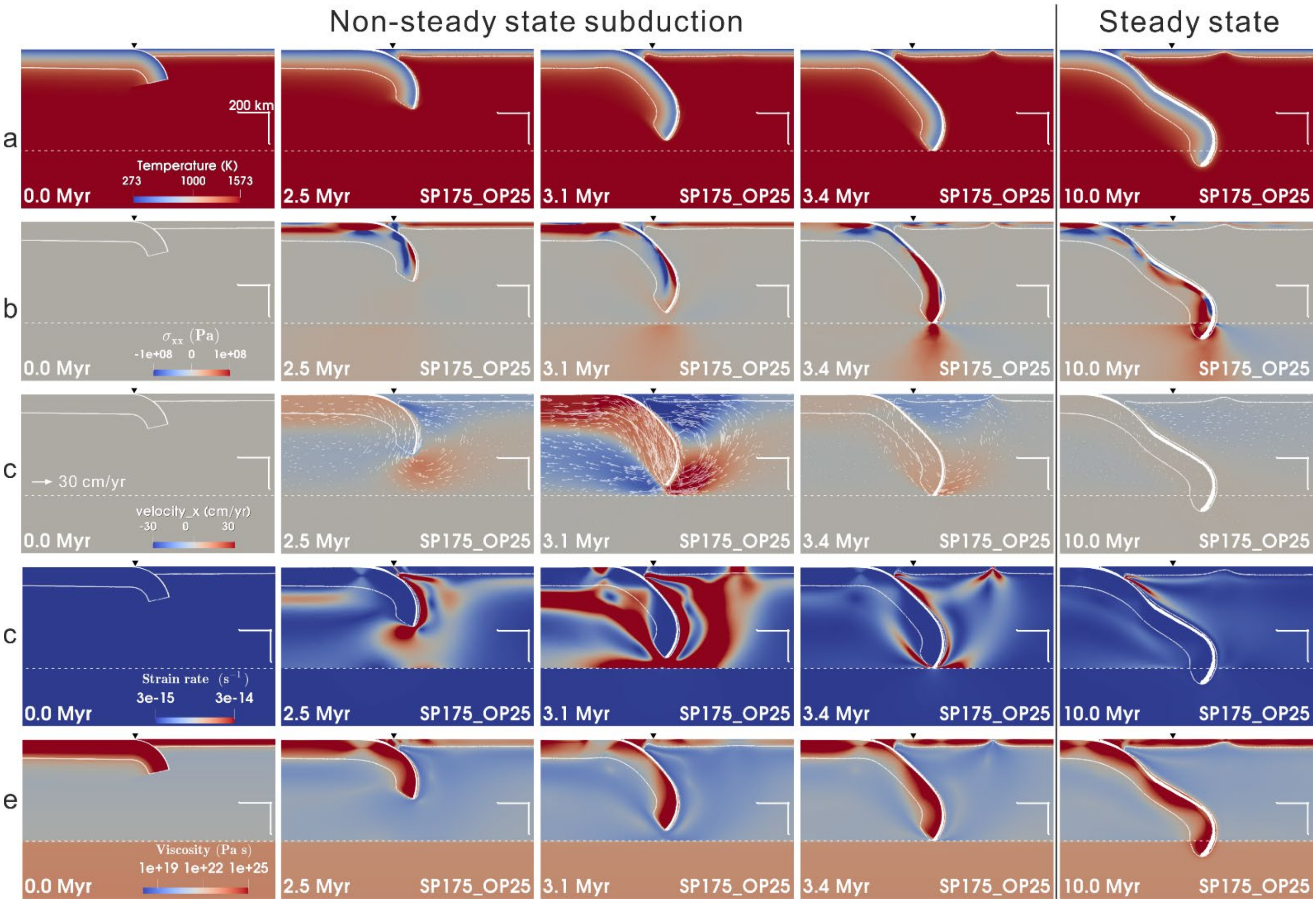

Figure 3. Simultaneous snapshots of a zoom-in to the region of active subduction in model SP175_OP25 showing: a) temperature,

b) horizontal component of the stress field, positive is extensional stress while negative is compressional stress, c) horizontal component of velocity field superimposed with velocity vectors, d) second invariant of strain rate, e) magnitude of viscosity. The downward black triangle at the surface marks the initial location of trench. The curved white solid line underneath the plate is the 1300 K isotherm, i.e., we take this as the bottom of the thermal lithosphere. The dashed white line marks the base of the transition zone at 660 km depth. The number with unit ‘Myr’ in the bottom left corner is the duration of the simulation. The right-angle scale bars above the transition zone represent 200 km in both horizontal and vertical direction.

3.2.1 Non-steady state subduction

Before the subducting plate starts to interact with the lower mantle around 3.3 Myr (Table 2), there is visible erosion in the mantle wedge (Figure 3-a). The horizontal component of the stress field indicates that the overriding plate portion away from the subducting plate is in a general high extensional stress field (> 50 MPa), leaving the portion close to the subducting plate in a general compressional stress state (Figure 3-b). The velocity vectors visualise a clockwise laminar mantle flow underlying the subducting plate and an anticlockwise poloidal flow underlying the overriding plate (Figure 3-c). The horizontal component of velocity field within the whole overriding plate is initially consistent laterally. As the slab sinking accelerates, the trenchward velocity of the overriding plate next to the trench increases faster than the trailing part of the overriding plate. This creates an increasing horizontal velocity difference within the overriding plate. In the corresponding area, a high strain rate region (Figure 3-d) and low viscosity (Figure 3-e) region at 3.1-3.4 Myr is observed marking the initiation of the rifting within the overriding plate.

3.2.2 Steady state subduction

After the subducting plate reaches the lower mantle, both the mantle wedge erosion and the initiated rift cools down and the thermal thickness of the overriding plate starts to recover. The horizontal component of the stress field within the overriding plate loses the general high extensional stress state and becomes mixed with a low magnitude of both compressional and extensional stress field. The velocity field indicates that the whole system decelerates to a slow-motion mode, where plates and mantle flow move with a low uniform velocity magnitude. Meanwhile, the high strain rate vanishes in the back-arc region and it is only observed in a limited area in the mantle wedge. The viscosity field within the overriding plate also recovers its stiffness. In summary, the mobility of the whole subduction system is inhibited in this stage and tectonics within the overriding plate is relatively silent compared with the non-steady state subduction stage.

3.3 Three types of stretching state within the overriding plate

The case described above has demonstrated the ability of a retreating trench to deform the overriding plate. Here we present the diversity of localised extension that trench retreat can bring about within the overriding plate. Three grades of stretching state within the overriding plate have been recognised (Table 2). Grade i) Minor extension. In the mantle wedge, convective mantle flux erodes part of the overriding plate’s bottom (Figure 4-a). Further away towards the overriding plate, observable but very limited thinning of the thermal lithosphere develops. Grade ii) Rifting. A higher magnitude of thermal erosion develops in the mantle wedge. While rifting extension forms during non-steady state subduction in the back-arc (Figure 4-b). The rift goes inactive during the steady state subduction. Grade iii) Spreading seafloor or break-up extension. In the mantle wedge, even higher magnitude of thermal erosion develops but no rifting extension forms. Further away towards the overriding plate, rifting extension develops and then breaks up into two parts forming a new oceanic floor during non-steady state subduction (Figure 4-c). The width of the opening seafloor can be as wide as ~250 km. During the steady state subduction, the break-up goes inactive due to the lack of consistent strong trench retreat.

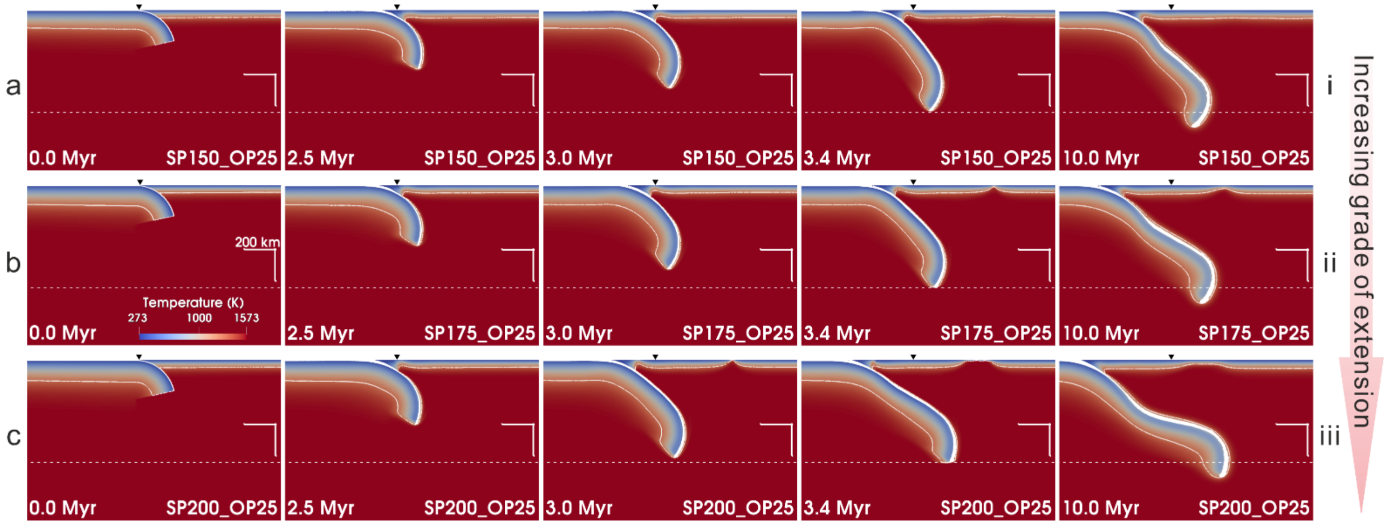

Figure 4. Simultaneous snapshots of the thermal field evolution of three cases, illustrating the differing stretching states within the overriding plate: a) minor extension (model SP150_OP25); b) rifting (model SP175_OP25); c) spreading seafloor (model SP200_OP25). All screenshots share the same temperature scale as is shown in first screenshot in row b.

To understand the deformation in the three stretching states, we track the second invariant of strain rate ($\dot{\varepsilon}_{II}$) in the back-arc region and plot it over time (Figure 5). It shows that for the five models that develop minor extension stretching state (Table 2), $\dot{\varepsilon}_{II}$ is always less than $2 \times 10^{-14}\, s^{-1}$ throughout the simulation. While for the two rifting extension models, $\dot{\varepsilon}_{II}$ can go beyond $2 \times 10^{-14}\, s^{-1}$ and reach the maximum value of ~$3.3 \times 10^{-13}\, s^{-1}$ when rift develops within the overriding plate. For the three break-up models, $\dot{\varepsilon}_{II}$ exceeds $3.3 \times 10^{-13}\, s^{-1}$ when the rifting ridge starts to spread in the back-arc. The strain rate quickly drops down to less than $1 \times 10^{-13}\, s^{-1}$ during steady state subduction, indicating that extensional deformation within the overriding plate gradually stops simultaneously.

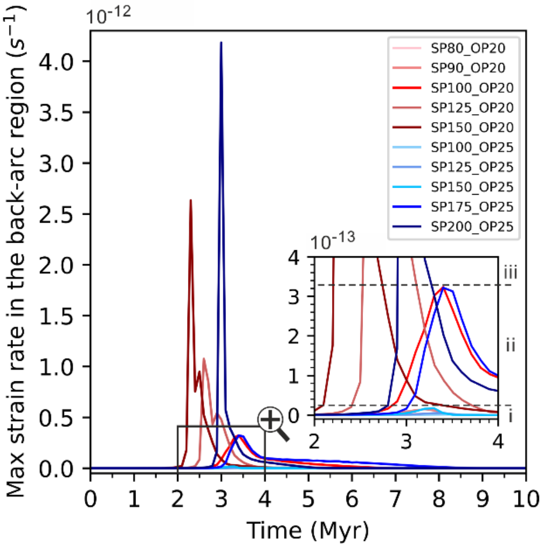

Figure 5. Maximum second invariant of strain rate through time in the back-arc region. The period from 2 to 4 Myr is enlarged to display the maximum strain rate corresponding to minor extension (Grade i) and to rift extension (Grade ii) that can be achieved throughout the simulation.

Matching the three stretching states with the trench retreat rate over time (Figure 2-a), we note that it takes a minimum magnitude of trench retreat rate (u_{rift}) to initiate rifting within a given overriding plate. The u_{rift} for $Age_{OP}^{0} = 20\,Myr$ and $Age_{OP}^{0} = 25\,Myr$ are ~19 cm/yr and ~27 cm/yr respectively. When the trench retreat rate exceeds u_{rift}, break-up extension develops following the rifting in the back-arc region. Take model SP200_OP25 for example, when the trench retreat rate reaches ~27 cm/yr at 2.9 Myr, the overriding plate starts to rift and $\dot{\varepsilon}_{II}$ is $1.8 \times 10^{-13}\,s^{-1}$ falling in the range of rift deformation (Figure 5). Then the trench retreat rate exceeds u_{rift} and break-up extension develops characterised by high $\dot{\varepsilon}_{II}$ greater than $3.3 \times 10^{-13}\,s^{-1}$ (Figure 5).

3.4 Regime diagram

Combining the above diagnostics and visualised output, we plot a regime diagram of overriding plate stretching state in response to different model setup (Figure 6-a). The diagram is divided into three parts based on the final stretching state of the overriding plate: i) minor extension, ii) rifting,

iii) spreading new seafloor. The diagram shows that with either increasing Age_{SP}^{0} (i.e., increasing $|u_{max}^{0-t_{660}}|$) or decreasing Age_{OP}^{0} (i.e., decreasing u_{rift}), a stronger extent of extension develops within the back-arc region.

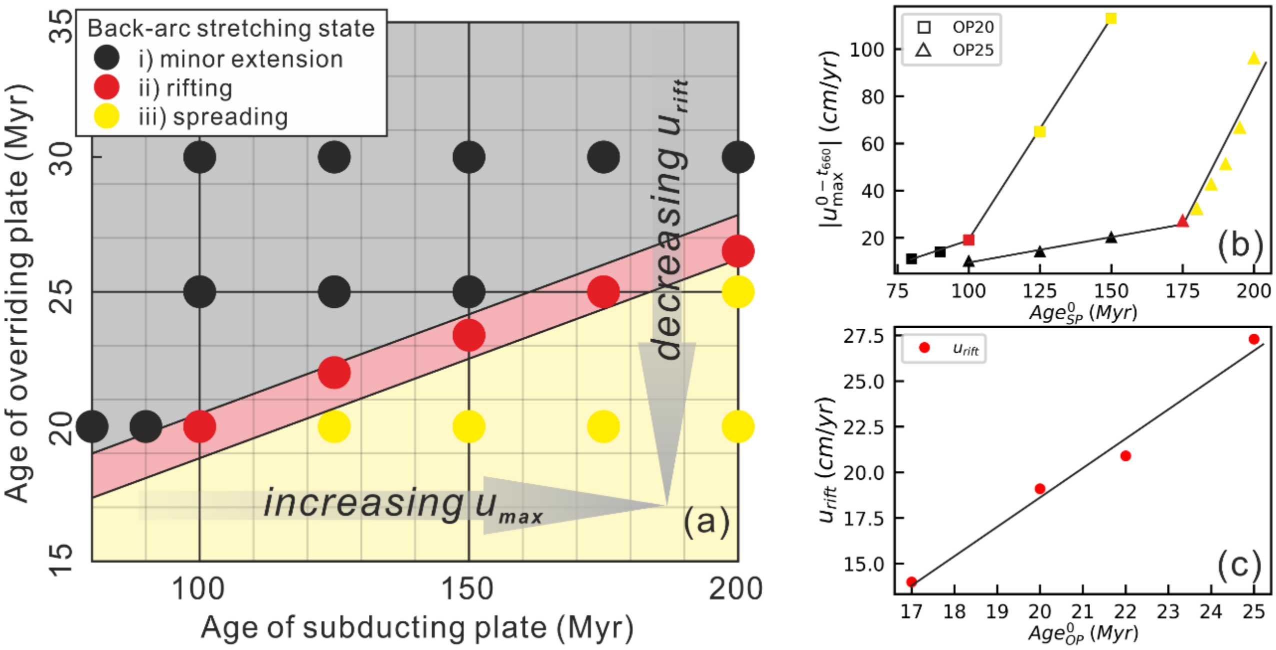

Figure 6. Regime diagram of back-arc extension and age dependency of trench motions. (a) Regime diagram of back-arc stretching state with varying Age_{SP}^{0} and Age_{OP}^{0}. Grey area with black dot models has minor extension in the back-arc region, while pink area with red dot models is rifting extension. The yellow area with gold dot models represents spreading back-arc. (b) The maximum trench retreat rate in response to Age_{SP}^{0}. (c) The minimum trench retreat rate to initiate rift extension within an overriding plate with an initial age of Age_{OP}^{0}. The colour of markers in (b) and (c) refer to the legend of back-arc stretching state in (a).

In summary, we propose that it takes a minimum magnitude of trench retreat rate u_{rift} to initiate rifting within a given overriding plate in these models. The $|u_{max}^{0-t_{660}}|$ depends on Age_{SP}^{0} for a given overriding plate (Figure 6-b), while the magnitude of u_{rift} depends on the strength of the overriding plate, i.e. Age_{OP}^{0} in this research (Figure 6-c). A steeper slope of $|u_{max}^{0-t_{660}}|$ against Age_{SP}^{0} is observed in models with spreading extension (Figure 6-b). This suggests that the strength of the original overriding plate is greatly weakened during rift extension and it becomes equivalent to a much younger overriding plate in terms of rheology.

Comparing $\left|u_{max}^{0-t_{660}}\right|$ and u_{rift}, we find that the results match well with the stretching state observed. i) If $u_{\max} < u_{\mathrm{rift}}$ then the overriding plate lithosphere has little extension and max $\dot{\varepsilon}_{II}$ is $3 \times 10^{-14}\ s^{-1}$. ii) If $u_{\max} \approx u_{\mathrm{rift}}$ the overriding plate rifts but would neither be torn apart nor spread, when $\dot{\varepsilon}_{II}$ ranges from $3 \times 10^{-14}\ s^{-1}$ to $3 \times 10^{-13}\ s^{-1}$. iii) If $u_{\max} > u_{\mathrm{rift}}$, the back-arc region rifts when the trench retreat rate reaches u_{rift}, then it breaks up into two parts and spreads after it exceeds u_{rift} with $\dot{\varepsilon}_{II}$ simultaneously exceeding $3 \times 10^{-13}\ s^{-1}$.

4. Discussion

4.1 Origin of the three stretching states in the overriding plate

The driving mechanism of how the trench retreats, and slab rollback induces extension within the overriding plate remains debated. Trench suction and non-uniform basal traction are two basic driving mechanisms. The stress field results show that a compressional stress field next to the subduction interface on the overriding plate's side prevails during the non-steady state subduction (Figure 3-b). This indicates that shortening, rather than extension, is the dominant deformation there, which excludes a direct correlation between trench suction at the subduction interface with focused back-arc extension. Similar shortening deformation at the subduction interface as the trench retreats is also reported in other research (Chen et al., 2016; Schellart and Moresi, 2013). However, the velocity field does show that mantle flow underlying the overriding plate is sucked into the wedge as the slab rolls back (Figure 3-c). So 'deep slab suction' rather than 'trench suction' may contribute to the back-arc extension by facilitating the mobility of mantle flow in the mantle wedge.

To understand the origin of the three overriding plate stretching states developed in this research, we need to study the mantle circulation underlying the overriding plate. During the non-steady state subduction, a strong anticlockwise poloidal flow develops underlying the overriding plate before the rift forms (Figure 3-c). Take models SP150_OP25, SP175_OP25 and SP200_OP25 for example, the flow could be decomposed into two components: focused upwelling from the transition zone; and trenchward horizontal flow underneath the overriding plate (Figure 7). These two differently directed flows correspond to the two end members of potential driving mechanisms accounting for the stretching state within the overriding plate: 1) upwelling thermal intrusion; and 2) lateral basal traction. As velocity difference is key to generate shear traction upon the overriding plate, we select the high velocity component areas ($\geq u_{rift}$) and analyse their correlation with the development of three stretching states within the overriding plate.

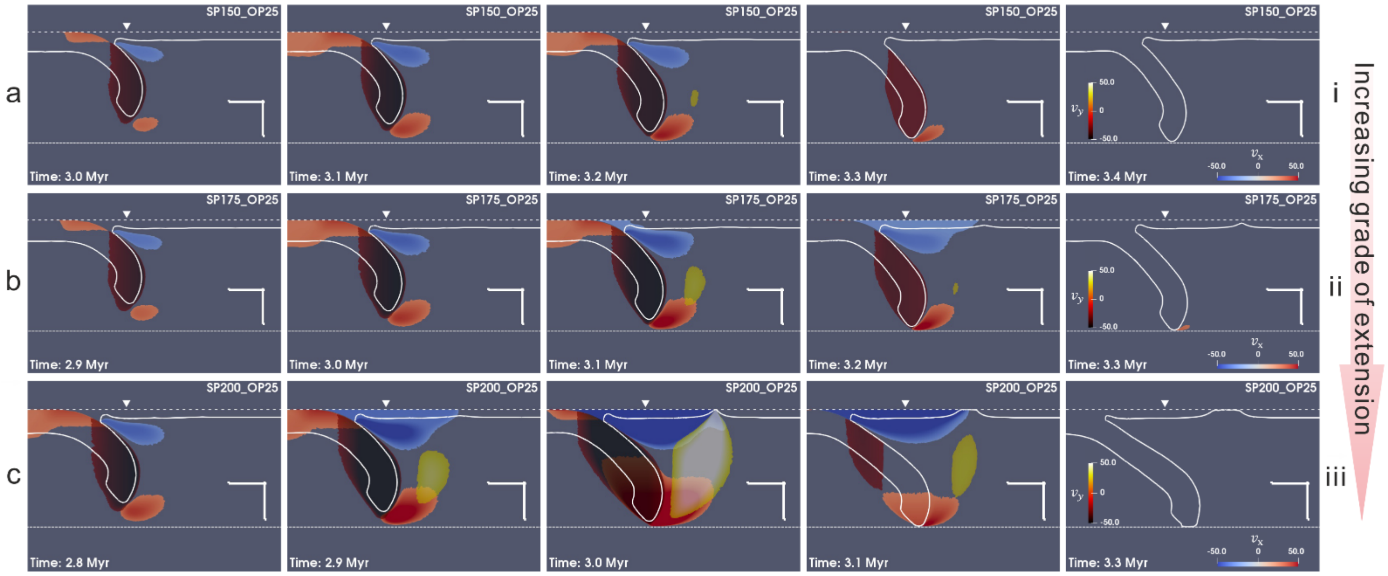

Figure 7. Snapshots of vertical and horizontal components of mantle circulation induced by slab roll-back. The vertical flow (u_y) and horizontal flow (u_x) are highlighted with two separate color legends (right most snapshot). Trenchward and downwelling motions are negative in the screenshots. Besides, all the visualised areas have a velocity magnitude higher than u_{rift} (~27 cm/yr for $Age_{OP}^{0} = 25\ Myr$) in the corresponding direction, i.e. either $|u_y| \geq u_{rift}, or\ |u_x| \geq u_{rift}$. The models i, ii, iii corresponds to the three stretching states described in Figure 4. The loose dashed line marks the surface while the dense dashed line is at 660 km depth (the base of the transition zone).

4.1.1 Lateral basal traction

The fast horizontal flow prevails over the upwelling component among all snapshots in figure 7. Initially, the trenchward horizontal flow forms in the mantle wedge underlying the overriding plate and extends laterally to ~500 km from the wedge corner (Figure 7). The spatial distribution indicates the existence of both lateral and vertical velocity gradient, which produce non-uniform magnitude of basal drag beneath the overriding plate. The wedge flow gradually drags the overlying overriding plate trenchward. This can be seen as the high velocity magnitude region extends up from the wedge to include the overriding plate (3.1 to 3.2 Myr in Figure 7-b and 2.8 to 3.1 Myr in Figure 7-c). Due to the non-uniform basal drag effect, the trenchward velocity difference within the overriding plate grows. This leads to a growing magnitude of accumulated extension which would end up with increasing stretching states within the overriding plate.

The magnitude of the horizontal flow can exceed 50 cm/yr for a short period (<1 Myr) in these models. Seismic anisotropy observations near slab edges beneath Tonga and Alaska subduction zones suggest comparable magnitude of rapid wedge flow, up to 90 cm/yr (Conder and Wiens, 2007; Jadamec and Billen, 2010). Here we propose that the non-uniform basal drag of the rapid wedge flow driven by rapid trench retreat plays a vital role in producing back-arc opening during subduction.

4.1.2 Upwelling thermal intrusion

Figure 7 shows that fast-upwelling mantle flow is observed in all three models though it lasts for no more than 0.3 Myr. The size of the fast-upwelling mantle body grows with Age_{SP}^{0}, indicating a stronger return flow. In model SP200_OP25, the upwelling even appears under the rift before it fades away as the non-steady state subduction ends (Figure 7-c). However, the high velocity upwelling flow is prone to strengthen the stretching within the overriding plate rather than initiating significant rifting extension. We state this because it is not observed to interact with the overriding plate for model SP175_OP25 which starts to rift at 3.2 Myr (Figure 7-b).

In summary, the basal traction induced by trench retreat, or slab rollback, is the main driving force to account for different magnitude of extension within the overriding plate in our models. While the upwelling mantle component may reinforce the extension.

4.2 Comparing with other back-arc extension models

Previous research indicates that fixing the trailing boundary condition of the overriding plate can increase the degree of focused back-arc extension in contrast to models with a free mobile overriding plate (Capitanio et al., 2010; Chen et al., 2016; Hertgen et al., 2020; Nakakuki and Mura, 2013; Schellart and Moresi, 2013). While introducing heterogeneity, e.g. weak zone, in the overriding plate (Currie et al., 2008; Nakakuki and Mura, 2013; Yang et al., 2019) or lowering the strength of the whole overriding plate (Capitanio et al., 2010) can cultivate thinning lithosphere or even spreading back-arc extension (Figure 8). In brief, it usually takes a fixed or a weakened overriding plate to produce back-arc extension incorporating a rift. By contrast, this research demonstrates the capability of producing an opening back-arc in a homogeneous (i.e. without an arbitrary weak zone) mobile overriding plate by increasing the magnitude of non-uniform basal drag underlying the overriding plate as the trench retreats rapidly.

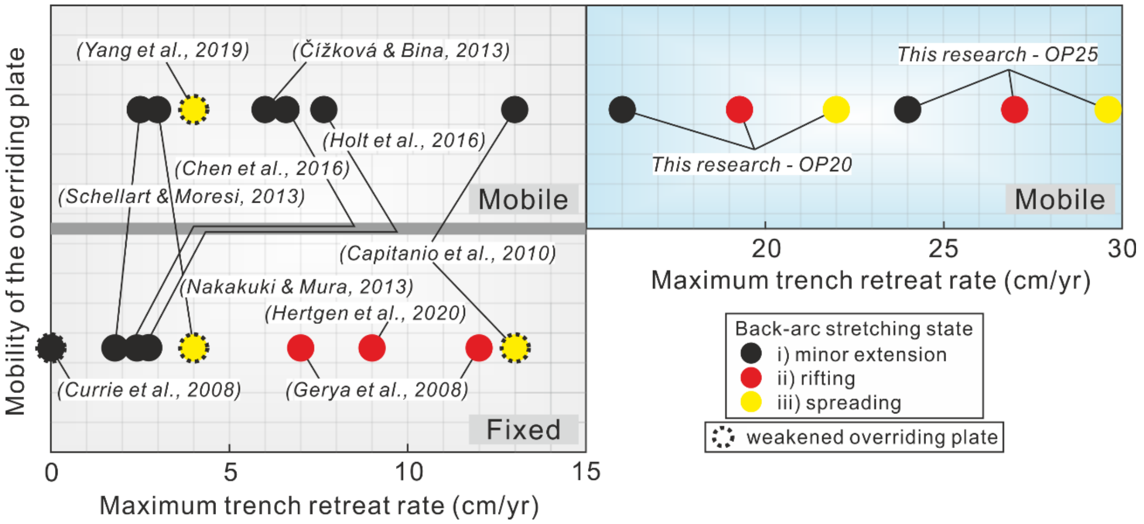

Figure 8. Summary of maximum trench retreat rate, mobility of the overriding plate and back-arc stretching state in previous research.

Previous models also indicate that maximum trench retreat is often reached at the end of non-steady state subduction when the slab starts to interact with the lower mantle (eg. Capitanio et al., 2010; Schellart and Moresi, 2013). The maximum trench retreat rate achieved during previous research presented in Figure 8 is ~13 cm/yr, which is lower than that of ~16 cm/yr observed in Tonga (Bevis et al., 1995). Considering that more than 90% of slabs have reached the lower mantle (van der Meer et al., 2018), the non-steady state subduction is transient relative to the following steady state subduction and its evolving history is poorly constrained by observations. Here we consider that the trench retreat rate can reach a high magnitude, at least for a short period (<1 Myr), during the non-steady state subduction phase, as produced in our models. This allows us to suggest the existence of a minimum trench retreat rate to initiate back-arc opening for a given overriding plate. The results imply that the role of non-steady state subduction and transient rapid trench retreat in promoting deformation within the overriding plate may be underestimated.

4.3 Comparing with subduction zones on Earth

Our results indicates that when the age of the subducting slab is old enough, it will allow the trench to retreat fast enough to initiate rift extension or even break-up extension in the back-arc region through non-uniform basal traction. This may explain why the subducting plate is always old, ranging from 55 Ma – 160 Ma, in subduction zones with a back-arc basin (Sdrolias and Müller, 2006).

We obtain a wide range of trench retreat rate by tuning Age_{SP}^{0}. However, modern observation shows that there is poor correlation between Age_{SP}^{0} and trench retreat rate (Heuret and Lallemand, 2005). Our result indicates that trench retreat rate loses its age dependency when the subducting slab starts to interact with the lower mantle. Considering that most subducting slabs on Earth have already reached or are approaching the lower mantle (van der Meer et al., 2018), it is then not surprising that a poor correlation is observed. The result suggests that different stages of subduction play an important role in controlling subduction kinematics and it may help us better understand observations on Earth.

We replicate three back-arc stretching states with a wide range of trench retreat rate. The extent of back-arc extension exhibits positive correlation with trench retreat rate. This matches well with subduction zones where trench retreat rates are higher than 5 cm/yr on Earth (Heuret and Lallemand, 2005; Schellart et al., 2008). Take the Lau-Havre-Taupo back-arc system for example, the width of the back-arc region narrows southward from ~500 km in Lau Basin to ~100 km along the Havre Trough and terminates in Taupo Volcanic Zone (Parson and Wright, 1996). The trench retreat rate correspondingly slows down from ~16 cm/yr to ~0 cm/yr along the Tonga-Kermadec trench (Schellart et al., 2008). While the thickness of the crust increases from ~5 km to ~25 km southward (Parson and Wright, 1996) and a high spreading rate is observed in northern Lau Basin at ~9.1 – 15.9 cm/yr (Bevis et al., 1995).

In our models that produce spreading back-arc, we find that the opening seafloor stops spreading after trench retreat rate drops to a low constant magnitude of ~3 cm/yr during steady state subduction (Figure 4-c). This may explain why some spreading back-arc stop spreading even when subduction continues. For example, the back-arc in Japan sea opened at ~21 Ma and ceased spreading since ~14 Ma during the Pacific Plate subduction (Tatsumi et al., 1990). The Japan subduction zone is still active while the present trench retreat rate is low at only ~0 cm/yr (Schellart et al., 2008).

We noted, our simplified models cannot reproduce the periodic opening process of the back-arc basin. Magnetic anomalies in opening back-arc regions indicate that the spreading tends to be periodic and consistent (Caratori Tontini et al., 2019; Eagles and Jokat, 2014) rather than abrupt and short-lived. During steady state subduction, the rifted back-arc region is likely to spread if high trench retreat rate is maintained rather than drops to the value of ~3 cm/yr seen in our models. This may be attributed to the limitation imposed by our 2D models which is discussed next.

4.4 Limitations

4.4.1 2D and 3D models

Trench retreat could generate convective mantle flow that includes poloidal and toroidal components. Two dimensional models, by their nature, can only produce poloidal flow. It is noted though, that poloidal flow is expected to dominate during the non-steady state subduction

(Funiciello et al., 2004). That is when high trench retreat rate develops in our models. Thus, a lack of toroidal flow might only have a limited impact on the formation of rapid trench retreat rate during non-steady state subduction.

However, as the subducting slab starts to interact with the lower mantle, trench retreat and upper mantle flow in 2D models are greatly inhibited (Figure 2-a, Figure 3-c). Trench retreat rate slows down by ~60% (Holt et al., 2015) and >70% in our models. This occurs because the subducting slab, combining with the viscosity jump into the lower mantle, disconnects the upper mantle flow on either side of the slab. While in 3D models, toroidal flow could efficiently transport mantle flow from the subducting plate side towards the overriding plate side - around the edges of slabs. Slab interaction with the lower mantle only slows down the trench retreat by 0% to ~33% in 3D models (Chen et al., 2016; Schellart et al., 2011). In this case where the slab is interacting with the lower mantle, the lack of toroidal flow causes a significant slowing down effect on the trench retreat rate and potentially also simultaneously inhibits back-arc extension. Thus, the lack of toroidal flow may not be neglected when slab starts to interact with the lower mantle.

4.4.2 Absolute value of trench retreat rate and $\boldsymbol{u_{rift}}$

This research aims to provide a guiding reference framework to correlate trench retreat rate and extent of extension in the back-arc region rather than provide precise predictions. Thus, the absolute value of trench retreat rate should be treated with caution. We note that while the older subducting plate ages (> 160 Ma) at trenches are presently not common on Earth (Müller et al., 2008), they provide us a way to self-consistently produce the varying trench retreat rates. Considering that there is a lot of uncertainty in terms of the strength of plates on Earth, the trench retreat rate it takes to initiate rift extension could vary greatly. Some of our models yield much higher trench retreat rates than observed, this may imply that either the rheology we used does not fully agree with real Earth or that current observation might be incomplete.

During non-steady state subduction, $\left|\overline{u_{trench}^{0-t_{660}}}\right|$ in our model (3.5-15.6 cm/yr) is in the same range as actual observations on Earth (0-16 cm/yr). While the maximum trench retreat rate obtained from the model (10-113 cm/yr) spans a much wider range than observations on Earth. The extremely high $\left|u_{max}^{0-t_{660}}\right|$ is achieved in spreading back-arc models after the back-arc lithosphere's rheology is reshaped by the emplaced rifting ridge. Similar abrupt acceleration is reported to exist in some rifting continental margins and it is controlled by the nonlinear decay of the strength force resisting rifting (Brune et al., 2016).

The u_{rift} for $Age_{OP}^{0} = 20\,Myr$ and $Age_{OP}^{0} = 25\,Myr$ are ~19 cm/yr and ~27 cm/yr separately, hinting that it can be difficult to initiate rifting extension in models $Age_{OP}^{0} > 20\,Myr$ with observed trench retreat rates on Earth. There are several parameters that could potentially lower the u_{rift} which is not addressed in this research, for example, inhibiting the mobility of the overriding plate or lowering the strength of the overriding plate.

5. Conclusion

The 2D thermo-mechanical self-consistent models demonstrate the capability of initiating back-arc rifting or spreading in a mobile and homogenous (no arbitrary weak zone) overriding plate with high enough trench retreat rate during subduction. A wide range of trench retreat rate is achieved by varying the initial age of the subducting plate at the trench for a given overriding plate. The models evolve from a non-steady state towards a steady state with the transition occurring when the subducting plate approaches the lower mantle. During non-steady state subduction, trench retreat rate accelerates and reaches its maximum value, which depends on the initial age of the subducting plate. In all, three types of stretching state were observed within the overriding plate: i) minor extension, where the overriding plate lithosphere remained generally unchanged; ii) rift extension, where the overriding plate would be rifted but not torn apart; iii) spreading extension, where back-arc is rifted and then breaks apart into two spreading parts. The results indicate that it takes a minimum trench retreat rate to initiate rift extension and a higher trench retreat rate to open the back-arc. The driving force in these models is suggested to be the non-uniform basal drag resulting from the mantle wedge flow driven by the rapid trench retreat. After the subducting plate reaches the lower mantle, the trench retreat rate drops to a constant magnitude around 3 cm/yr and loses the dependency on the initial age of subducting plate. Meanwhile, simultaneously the back-arc extension stops when trench retreat rate slows down during the steady state subduction. This suggests that different stages of subduction play an important role in controlling subduction kinematics and it may help us better understand why there is poor correlation between trench retreat rate and the age of subducting plate.

In addition to the previous understanding of back-arc extension, we propose that high enough trench retreat rate can initiate a rift or spreading back-arc extension through non-uniform basal drag even when the overriding plate is mobile.

Acknowledgement

Duo Zhang provided constructive suggestions. We acknowledge the support of Advanced Research Computing at Cardiff (ARCCA) and the Supercomputing Wales project, which is part-funded by the European Regional Development Fund (ERDF) via the Welsh Government. Zhibin Lei also thanks the China Scholarship Council (CSC) for supporting the Ph.D. studentship and Cardiff University for an overseas fee waiver award.

References

Alsaif, M., Garel, F., Gueydan, F., Davies, D.R., 2020. Upper plate deformation and trench retreat modulated by subduction-driven shallow asthenospheric flows. Earth Planet. Sci. Lett. 532. https://doi.org/10.1016/j.epsl.2019.116013

Bevis, M., Taylor, F.W., Schutz, B.E., Recy, J., Isacks, B.L., Helu, S., Singh, R., Kendrick, E., Stowell, J., Taylor, B., Calmantli, S., 1995. Geodetic observations of very rapid convergence and back-arc extension at the tonga arc. Nature 374, 249–251. https://doi.org/10.1038/374249a0

Brune, S., Williams, S.E., Butterworth, N.P., Müller, R.D., 2016. Abrupt plate accelerations shape rifted continental margins. Nature 536, 201–204. https://doi.org/10.1038/nature18319

Butterworth, N.P., Quevedo, L., Morra, G., Müller, R.D., 2012. Influence of overriding plate geometry and rheology on subduction. Geochemistry, Geophys. Geosystems 13, 1–15. https://doi.org/10.1029/2011GC003968

Capitanio, F.A., Stegman, D.R., Moresi, L.N., Sharples, W., 2010. Upper plate controls on deep subduction, trench migrations and deformations at convergent margins. Tectonophysics 483, 80–92. https://doi.org/10.1016/j.tecto.2009.08.020

Caratori Tontini, F., Bassett, D., de Ronde, C.E.J., Timm, C., Wysoczanski, R., 2019. Early evolution of a young back-arc basin in the Havre Trough. Nat. Geosci. 12, 856–862. https://doi.org/10.1038/s41561-019-0439-y

Chen, Z., Schellart, W.P., Strak, V., Duarte, J.C., 2016. Does subduction-induced mantle flow drive backarc extension? Earth Planet. Sci. Lett. 441, 200–210. https://doi.org/10.1016/j.epsl.2016.02.027

Chertova, M. V., Geenen, T., Van Den Berg, A., Spakman, W., 2012. Using open sidewalls for modelling self-consistent lithosphere subduction dynamics. Solid Earth 3, 313–326. https://doi.org/10.5194/se-3-313-2012

Christeson, G.L., Barth, G.A., 2015. Aleutian basin oceanic crust. Earth Planet. Sci. Lett. 426, 167–175. https://doi.org/10.1016/j.epsl.2015.06.040

Čížková, H., Bina, C.R., 2013. Effects of mantle and subduction-interface rheologies on slab stagnation and trench rollback. Earth Planet. Sci. Lett. 379, 95–103. https://doi.org/10.1016/j.epsl.2013.08.011

Conder, J.A., Wiens, D.A., 2007. Rapid mantle flow beneath the Tonga volcanic arc. Earth Planet. Sci. Lett. 264, 299–307. https://doi.org/10.1016/j.epsl.2007.10.014

Currie, C.A., Huismans, R.S., Beaumont, C., 2008. Thinning of continental backarc lithosphere by flow-induced gravitational instability. Earth Planet. Sci. Lett. 269, 436–447. https://doi.org/10.1016/j.epsl.2008.02.037

Davies, D.R., Wilson, C.R., Kramer, S.C., 2011. Fluidity: A fully unstructured anisotropic adaptive mesh computational modeling framework for geodynamics. Geochemistry, Geophys. Geosystems 12, n/a-n/a. https://doi.org/10.1029/2011GC003551

Di Giuseppe, E., Van Hunen, J., Funiciello, F., Faccenna, C., Giardini, D., 2008. Slab stiffness control of trench motion: Insights from numerical models. Geochemistry, Geophys. Geosystems 9, 1–19. https://doi.org/10.1029/2007GC001776

Eagles, G., Jokat, W., 2014. Tectonic reconstructions for paleobathymetry in Drake Passage. Tectonophysics 611, 28–50. https://doi.org/10.1016/j.tecto.2013.11.021

Elsasser, W.M., 1971. Sea-floor spreading as thermal convection. J. Geophys. Res. 76, 1101–1112. https://doi.org/10.1029/JB076i005p01101

Fouquet, Y., Stackelberg, U. Von, Charlou, J.L., Donval, J.P., Erzinger, J., Foucher, J.P., Herzig, P., Mühe, R., Soakai, S., Wiedicke, M., Whitechurch, H., 1991. Hydrothermal activity and metallogenesis in the Lau back-arc basin. Nature 349, 778–781. https://doi.org/10.1038/349778a0

Fowler, C., 2005. The Solid Earth: An Introduction to Global Geophysics. Cambridge Univ. Press, Cambridge, U. K.

Funiciello, F., Faccenna, C., Giardini, D., 2004. Role of lateral mantle flow in the evolution of subduction systems: Insights from laboratory experiments. Geophys. J. Int. 157, 1393–1406. https://doi.org/10.1111/j.1365-246X.2004.02313.x

Garel, F., Goes, S., Davies, D.R., Davies, J.H., Kramer, S.C., Wilson, C.R., 2014. Interaction of subducted slabs with the mantle transition-zone: A regime diagram from 2-D thermo-mechanical models with a mobile trench and an overriding plate. Geochemistry, Geophys. Geosystems 15, 1739–1765. https://doi.org/10.1002/2014GC005257

Gerya, T. V., Connolly, J.A.D., Yuen, D.A., 2008. Why is terrestrial subduction one-sided? Geology 36, 43–46. https://doi.org/10.1130/G24060A.1

Hertgen, S., Yamato, P., Guillaume, B., Magni, V., Schliffke, N., Hunen, J., 2020. Influence of the thickness of the overriding plate on convergence zone dynamics. Geochemistry, Geophys. Geosystems 21. https://doi.org/10.1029/2019GC008678

Hessler, A.M., Sharman, G.R., 2018. Subduction zones and their hydrocarbon systems. Geosphere 14, 2044–2067. https://doi.org/10.1130/GES01656.1

Heuret, A., Lallemand, S., 2005. Plate motions, slab dynamics and back-arc deformation. Phys. Earth Planet. Inter. 149, 31–51. https://doi.org/10.1016/j.pepi.2004.08.022

Holt, A.F., Becker, T.W., 2017. The effect of a power-law mantle viscosity on trench retreat rate. Geophys. J. Int. 208, 491–507. https://doi.org/10.1093/gji/ggw392

Holt, A.F., Becker, T.W., Buffett, B.A., 2015. Trench migration and overriding plate stress in dynamic subduction models. Geophys. J. Int. 201, 172–192. https://doi.org/10.1093/gji/ggv011

Jadamec, M.A., Billen, M.I., 2010. Reconciling surface plate motions with rapid three-dimensional mantle flow around a slab edge. Nature 465, 338–341. https://doi.org/10.1038/nature09053

Jolivet, L., Tamaki, K., Fournier, M., 1994. Japan Sea, opening history and mechanism: a synthesis. J. Geophys. Res.

99. https://doi.org/10.1029/93jb03463

Kósik, S., Bebbington, M., Németh, K., 2020. Spatio-temporal hazard estimation in the central silicic part of Taupo Volcanic Zone, New Zealand, based on small to medium volume eruptions. Bull. Volcanol. 82. https://doi.org/10.1007/s00445-020-01392-6

Kramer, S.C., Wilson, C.R., Davies, D.R., 2012. An implicit free surface algorithm for geodynamical simulations. Phys. Earth Planet. Inter. 194–195, 25–37. https://doi.org/10.1016/j.pepi.2012.01.001

McKenzie, D.P., Roberts, J.M., Weiss, N.O., 1974. Convection in the earth's mantle: towards a numerical simulation. J. Fluid Mech. 62, 465. https://doi.org/10.1017/S0022112074000784

Meyer, C., Schellart, W.P., 2013. Three-dimensional dynamic models of subducting plate-overriding plate-upper mantle interaction. J. Geophys. Res. Solid Earth 118, 775–790. https://doi.org/10.1002/jgrb.50078

Morley, C.K., Alvey, A., 2015. Is spreading prolonged, episodic or incipient in the Andaman Sea? Evidence from deepwater sedimentation. J. Asian Earth Sci. 98, 446–456. https://doi.org/10.1016/j.jseaes.2014.11.033

Müller, R.D., Sdrolias, M., Gaina, C., Roest, W.R., 2008. Age, spreading rates, and spreading asymmetry of the world's ocean crust. Geochemistry, Geophys. Geosystems 9, 1–19. https://doi.org/10.1029/2007GC001743

Nakakuki, T., Mura, E., 2013. Dynamics of slab rollback and induced back-arc basin formation. Earth Planet. Sci. Lett. 361, 287–297. https://doi.org/10.1016/j.epsl.2012.10.031

Parson, L.M., Wright, I.C., 1996. The Lau-Havre-Taupo back-arc basin: A southward-propagating, multi-stage evolution from rifting to spreading. Tectonophysics 263, 1–22. https://doi.org/10.1016/S0040-1951(96)00029-7

Schellart, W.P., Moresi, L., 2013. A new driving mechanism for backarc extension and backarc shortening through slab sinking induced toroidal and poloidal mantle flow: Results from dynamic subduction models with an overriding plate. J. Geophys. Res. Solid Earth 118, 3221–3248. https://doi.org/10.1002/jgrb.50173

Schellart, W.P., Stegman, D.R., Farrington, R.J., Moresi, L., 2011. Influence of lateral slab edge distance on plate velocity, trench velocity, and subduction partitioning. J. Geophys. Res. Solid Earth 116, 1–15. https://doi.org/10.1029/2011JB008535

Schellart, W.P., Stegman, D.R., Freeman, J., 2008. Global trench migration velocities and slab migration induced upper mantle volume fluxes: Constraints to find an Earth reference frame based on minimizing viscous dissipation. Earth-Science Rev. 88, 118–144. https://doi.org/10.1016/j.earscirev.2008.01.005

Sdrolias, M., Müller, R.D., 2006. Controls on back-arc basin formation. Geochemistry, Geophys. Geosystems 7. https://doi.org/10.1029/2005GC001090

Sleep, N.H., Toksöz, M.N., 1971. Evolution of Marginal Basins. Nature 233, 548–550. https://doi.org/10.1038/233548a0

Stegman, D.R., Freeman, J., Schellart, W.P., Moresi, L., May, D., 2006. Influence of trench width on subduction hinge retreat rates in 3-D models of slab rollback. Geochemistry, Geophys. Geosystems 7, n/a-n/a. https://doi.org/10.1029/2005GC001056

Tatsumi, Y., Maruyama, S., Nohda, S., 1990. Mechanism of backarc opening in the Japan Sea: role of asthenospheric injection. Tectonophysics 181, 299–306. https://doi.org/10.1016/0040-1951(90)90023-2

Taylor, B., Zellmer, K., Martinez, F., Goodliffe, A., 1996. Sea-floor spreading in the Lau back-arc basin. Earth Planet. Sci. Lett. 144, 35–40. https://doi.org/10.1016/0012-821x(96)00148-3

Turcotte, D.L., Schubert, G., 2002. Geodynamics. Cambridge Univ. Press, Cambridge, U. K.

van der Meer, D.G., van Hinsbergen, D.J.J., Spakman, W., 2018. Atlas of the underworld: Slab remnants in the mantle, their sinking history, and a new outlook on lower mantle viscosity. Tectonophysics 723, 309–448. https://doi.org/10.1016/j.tecto.2017.10.004

Yang, T., Moresi, L., Gurnis, M., Liu, S., Sandiford, D., Williams, S., Capitanio, F.A., 2019. Contrasted East Asia and South America tectonics driven by deep mantle flow. Earth Planet. Sci. Lett. 517, 106–116. https://doi.org/10.1016/J.EPSL.2019.04.025